www.ijemr.net ISSN (ONLINE): 2250-0758, ISSN (PRINT): 2394-6962

Volume-8, Issue-4, August 2018

International Journal of Engineering and Management Research

Page Number: 218-225

A Study of EPR_2 and Magnetic Properties at Low Temperatures

Dr. Pawan Kumar
Associate Professor, Department of Physics, Meerut College, Meerut, INDIA

Corresponding Author: drpkmc@gmail.com

ABSTRACT

CuCl2 • $2NC_5H_5$, which is regarded as one of the best known uniform spin-1/2 Heisenberg antiferromagnetic chain systems, was studied using electron paramagnetic resonance (EPR) and neutron diffraction techniques. According to our findings, $CuCl_2$ • $2NC_5H_5$ undergoes a magnetically ordered spiral state transition with Q = (0.5, 0.4, 0.5) r.l.u. at TN = 1.12 K, according to our findings. The zigzag interchange contacts were demonstrated to cause geometrical frustration, which influenced the ordered moment per Cu^2+ and EPR characteristics, notably the angular dependency of the line width. The EPR parameters' temperature sensitivity is explored.

Keywords-- Low Temperatures, EPR Properties, Magnetic Structure, Chain System

I. INTRODUCTION

In low-dimensional spin magnets, quantum fluctuations are considerably increased, making these systems excellent for testing many theoretical principles of quantum magnetism. One of these paradigm models is an isotropic spin-1/2 Heisenberg antiferromagnetic (AF) chain with uniform nearest-neighbor exchange coupling. Its ground state is a spin singlet in a zero field, and its spin dynamics are dictated by a gapless two-particle continuum of spin-1/2 excitations known as siphons. The Bethe ansatz can be used to compute the spinon excitation spectrum. Because the spin-1/2 chain is crucial, even a minor disruption can significantly alter the system's fundamental features, including its spin dynamics. For example, the presence of alternating (staggered) Dzyaloshinskii-Moriya (DM) interaction may result in a field-induced energy gap of $\sim H^{2/3}$ (H is the applied magnetic field), with sine-Gordon solitons and their bound states, breathers, forming the excitation spectrum. High-field electron spin resonance spectroscopy has definitely confirmed the presence of such excitations. A minimum in the gap at the soliton-magnon crossover in the vicinity of the magnetization saturation field was also discovered to be due to the staggered DM interaction.

One of the earliest spin-1/2 Heisenberg AF chain systems is $Cu(py)_2Cl_2$ ($CuCl_2$ • $2NC_5H_5$).Despite its extensive history, the system continues to draw a great deal of interest. We investigate the low-energy spin dynamics and magnetic structure of $Cu(py)_2Cl_2$ using electron paramagnetic resonance (EPR) and neutron diffraction techniques.

II. EXPERIMENTAL

$Cu(py)_2Cl_2$ belongs to the monoclinic P $2_1/n$ space group, with a = 16.967 A, b = 8.559 A, c = 3.847 A, and $\beta = 91.98^o$, as well as two formula units (Z = 2) each cell. Its crystal structure is depicted schematically in Figure 1. The unit cell comprises two magnetic Cu^{2+} ions (labelled A and B in Fig. 1) with coordinates of (0, 0, 0) and (1/2, 1/2, 1/2), respectively; Cu^{2+} chains run in the c direction. The molecule has a small intrachain exchange interaction of roughly 0.56 K and a large intrachain exchange interaction of J/k_B = 27.3 K. The system transitions into a three-dimensional (3D) ordered state when T_N = 1.12 K.

$Cu(py)_2Cl_2$ single crystals were grown from solution at the ETH Zürich using a slow-evaporation method. We used these crystals for our EPR experiments. Employed samples with a typical diameter of 2 mm^3. At a frequency of 9.4 GHz, the spectra were measured using an X-band Bruker Elexsys E500 EPR spectrometer. Angular dependences were measured with a precision of greater than a factor $\pm 1^{\circ}$. An Oxford Instruments helium-4 flow-type cryostat (model ESR900) with the lowest accessible temperature of 2 K was installed in the spectrometer. A unique EPR probe has been designed and built for reliable temperature measurements Figure. 2. The probe is made of a quartz tube with an inner and outer diameter of 1 mm and 4 mm, respectively. On a flat platform at the bottom of

ISSN (ONLINE): 2250-0758, ISSN (PRINT): 2394-6962

the probe, a temperature sensor (Lakeshore bare chip Cernox resistor, model CX-1050-BC-HT) is placed. A four-point technique using a Lakeshore 340 bridge is used to measure the temperature. The temperature sensor was in direct thermal contact with the sample, which was attached to the platform using Apiezon-N vacuum grease. The temperature sensor put in the probe had no appreciable parasitic contribution to the EPR spectra (or cavity damping).

The neutron-diffraction measurements were carried out at the Institute Laue-Langevin using the D10 four-circle diffractometer (Grenoble, France). A pyrolytic graphite (PG) monochromator gave a neutron wavelength of λ =2.367 A. In two separate arrangements, two different data sets were gathered. The first, obtained using a multidetector, attempted to refine the crystal structure at low temperatures. The second was gathered with a single detector and a PG analyzer, and was tuned for background reduction. It was put to use for the determination of the magnetic structure A dilution refrigerator with a base temperature of T = 100 mK was used to gather the data.

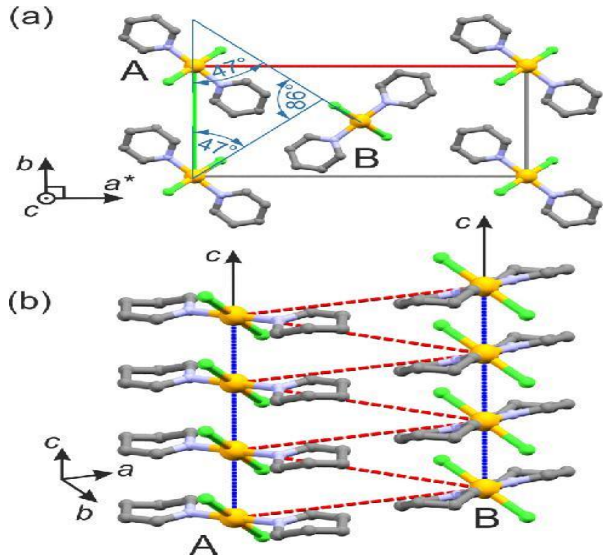

Figure 1: depicts a schematic representation of the $Cu(py)_2Cl_2$ crystal structure. Yellow, green, cyan, and grey represent the Cu, Cl, N, and C atoms, respectively. For the sake of clarity, the hydrogen atoms are not visible. The two distinct Cu^{2+} sites are denoted by the letters A and B. (For details, see the text).

III. DISCUSSIONS

From 300 to 2 K, the temperature dependency of the EPR spectra for $H \quad a^*$, $H \quad b$, and $H\,c$, was measured.

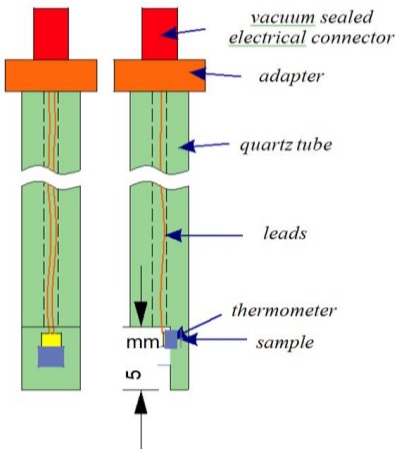

Figure 2: Front and side views of the EPR probe according to the schematic

ISSN (ONLINE): 2250-0758, ISSN (PRINT): 2394-6962

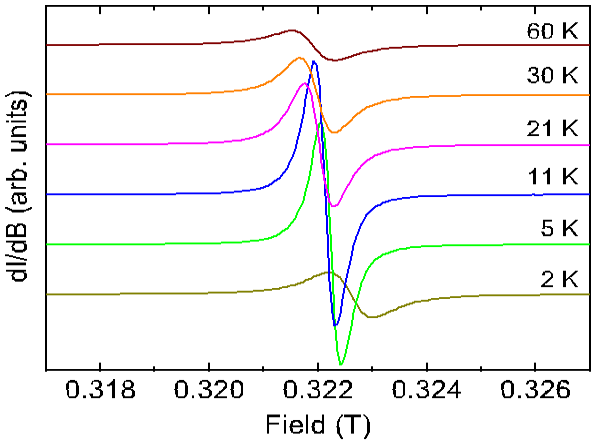

Figure 3: $Cu(py)_2Cl_2$ EPR spectra obtained at 2, 5, 11, 21, 30, and 60 K with magnetic field H b are shown in For the sake of clarity, the data has been offset

A single resonance line could be seen for all sample orientations. Figure 3 shows examples of EPR spectra for H b acquired at various temperatures. A Lorentzian fit function was used to describe the spectra, and the line width (full width at half maximum, FWHM) and resonance field were calculated from the fit results. The g factors and line widths at room temperature are presented in Table I.

Figure 4 shows the line width vs. temperature curves for H a*, H b, and H c.

According to the data, the EPR line width exhibited comparable behaviour in all three magnetic field directions. Starting at room temperature, the line widths decrease gradually, with a steeper slope below $T \sim J/k_B$ = 27.3 K and a minimum at T^* ~7.6 K. Short-range 3D correlations become substantial when temperature drops, resulting in low-temperature line-broadening reaching TN = 1.12 K (Fig. 4). The improvement of 3D correlations leads to a significant low-temperature change in the resonance field Figure-5.

The temperature range $T^* < T < J/k_B$ is now the focus of our attention. The magnetic properties of $Cu(py)_2Cl_2$ at these temperatures are determined by short-range correlations within the chains. In a perfect uniform spin-1/2 Heisenberg chain system with magnetically isotropic interactions, the EPR response should be a single absorption peak with zero line width at T = 0 K. Spin-spin correlations, on the other hand, result in a broadening of the EPR line in the presence of magnetic anisotropy. For spin-1/2 Heisenberg AF chains, the EPR line width is given as according to the low-temperature EPR theory

$$= _0 + n\pi^3\lambda^2 T, \qquad (1)$$

Table 1: shows the room-temperature parameters of the EPR absorption lines for all three magnetic field orientations

	H a*	H b	H c
g	2.0964(3)	2.0868(3)	2.1938(3)
(mT)	1.56	1.43	1.94

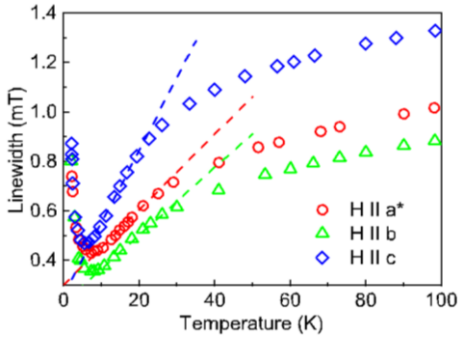

Figure 4: shows the EPR line width's temperature dependence. The data for H a*, H b, and H c are shown by the red, green, and blue symbols, respectively. The dashed lines indicate linear fits in the range $T^* < T < J/k_B$ using Eq. (1). (See the text for details)

ISSN (ONLINE): 2250-0758, ISSN (PRINT): 2394-6962

Where n = 2 or 4 corresponds to magnetic fields applied perpendicular to or parallel to the anisotropy axis, respectively, 0 is an offset, $\lambda \sim \delta/J$ for δ/J , and δ is the anisotropy parameter We calculated δ and 0 for each magnetic field direction based on the slope of the line width vs temperature. Table II shows the values that were discovered.

As can be seen, the anisotropy values are in the mK range and can be explained by the presence of small dipole-dipole interactions in this molecule. $Cu(py)_2Cl_2$ is thus an excellent realization of an isotropic spin-1/2 Heisenberg AF chain system above T_N.

At two temperatures, 300 and 10 K, the EPR angular dependency was determined (the sample was rotated along the c axis while the magnetic field was applied in the a*b plane). Figures 6 and 7 demonstrate the related angular dependences of the g factor and EPR line width, respectively.

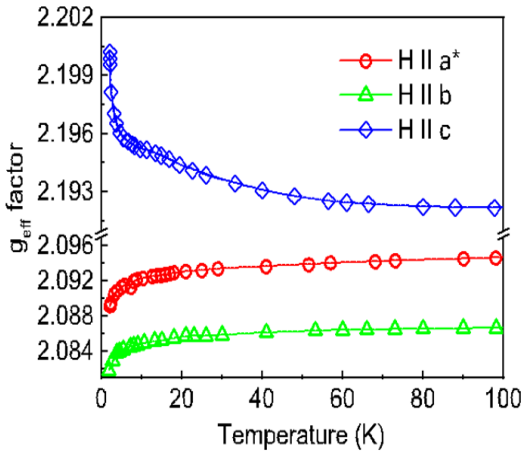

Figure 5: The effective *g* factors are temperature dependent. The data for *H* a, *H* b, and *H* c is represented by red circles, green triangles, and blue diamonds, respectively. Lines act as eye guides

Table 2: The parameters were retrieved from the EPR line width temperature dependency fit (Figure. 4) using Eq (1).

	H a*	*H* b	*H* c
$_0$ (mT)	0.3	0.23	0.26
δ (mK)	11	10	15

$Cu(py)_2Cl_2$ has two magnetic sites, *A* and *B* (Fig. 1), which contribute to the previously mentioned single EPR absorption with g factor.

$$g = \tfrac{1}{2}(g_A + g_B),$$

The effective *g* factors for sites *A* and *B* are *gA* and *gB*, respectively. *gA* and *gB*, on the other hand, can be written as

$$g_A^2 = g_{A,}^2 \cos^2(\theta + \varphi) + g_{A,}^2{}_{\perp} \sin^2(\theta + \varphi) \qquad (2)$$

and

$$g_B^2 = g_{B,}^2 \cos^2(\theta + \psi) + g_{B,}^2{}_{\perp} \sin^2(\theta + \psi), \qquad (3)$$

(and are the effective angles for each individual site, accounting for the tilting of the anisotropy axis from the an axis). Assuming that the only difference between the two sites is their orientation in relation to the unit-cell axes, one can write

ISSN (ONLINE): 2250-0758, ISSN (PRINT): 2394-6962

$$g = \frac{1}{2^{\perp}} \sqrt{g^2 \cos^2(\theta + \varphi) + g^2 \sin^2(\theta + \varphi)}$$

$$+ \frac{1}{2} \sqrt{g^2 \cos^2(\theta \quad \psi) \quad g^2 \sin^2(\theta \quad \psi)}. \quad (4)$$

We extract g and g by fitting the angular dependence of the g component with Eq. (4). The fit results are represented by dashed lines in Fig. 6, and the g factors are listed in Table 3.

Let's look at the linewidth's angular dependencies now. There are two maxima for both temperatures, at $\theta \sim 50^{\circ}$ and $\sim 135^{\circ}$, which correspond to the scenario when the magnetic field is strongest.

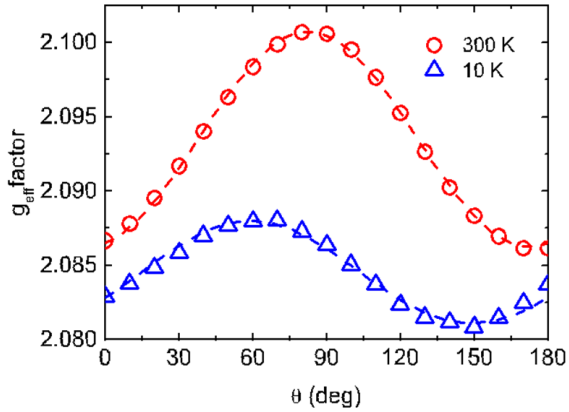

Figure 6: shows the angular dependency of the g factor at 300 and 10 K. On the c axis, the sample was rotated. In the a^* b plane, a magnetic field was applied. H b has a rotation angle of θ is defined as 0° and hence H a^* has a rotation angle of $\theta = 90^{\circ}$

The results acquired at 300 and 10 K are represented by red circles and blue triangles, respectively.

The fit results using Eq. are shown by the dashed lines (4).

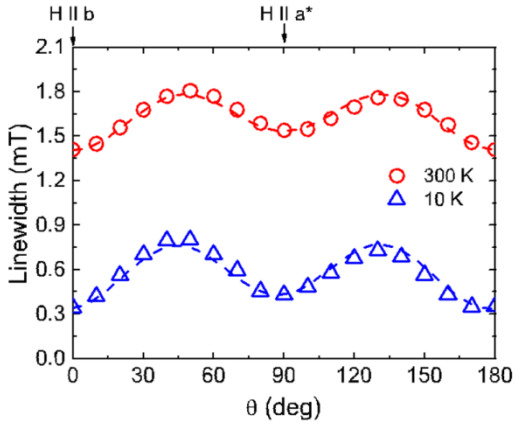

Figure 7: The EPR line width was measured at 300 and 10 K and found to be angularly dependent. On the c axis, the sample was rotated. A magnetic field was applied in the a^* b plane. The dashed lines reflect the results of fitting the experimental data using Eq (5)

One Cu^{2}+ site has a field applied in the basal plane produced by Cl^{-} ligands, while another has a field applied perpendicular to it [Fig. 1(a)]. This is a fascinating observation, and it suggests that frustrated zigzag interchain coupling may play a role, resulting in a no collinear magnetic structure below *TN* (as we show below).

Two expected EPR lines from different Cu^{2}+ sites were unable to be resolved. Let's look at the angular dependence of the line width to see what we can learn. The EPR line width behaviour can be stated as follows, similar to that in Ref.

ISSN (ONLINE): 2250-0758, ISSN (PRINT): 2394-6962

$$= \text{chain} + \frac{1}{4}\frac{(g_A - g_B)^2 \mu_B H^2}{h\omega^{-}_h}, \qquad (5)$$

ω_h is the frequency of interchain hopping, and chain =

$_i$ + $_a \sin(\theta)$ ($_i$ and $_a$ are the isotropic and

2 and 3 determine the anisotropic and anisotropic components of the linewidth, respectively, where H is the resonance field. The fit findings are represented by dashed lines in Fig. 7 (the fitting revealed h = 13.5 and 4.1 GHz for 300 and 10 K, respectively, and additional fitting values are listed in Table III). Both temperatures should be considered.

$|(g_A - g_B)|\mu_B H/h\omega^{-}_h < 1$, i.e.,

Table 3: A list of the parameters used in Eq. 7 to suit the EPR linewidth angular dependency (Fig. 7) Eq (5).

	300K	2K
g	2.072(1)	2.065(1)
$g_\perp$	2.115(1)	2.103(1)
H (mT)	322	322
i (mT)	1.41	0.34
$_a$ (mT)	0.13	0.09
φ, °	42.7	70.6
ψ, °	42.7	65.9
ω_h (GHz)	–	–
	13.5	4.1

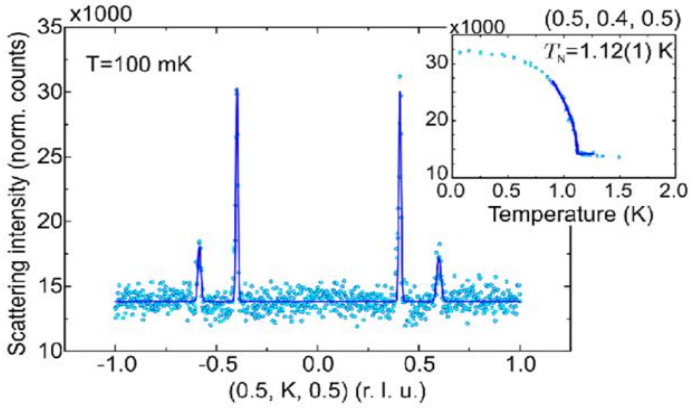

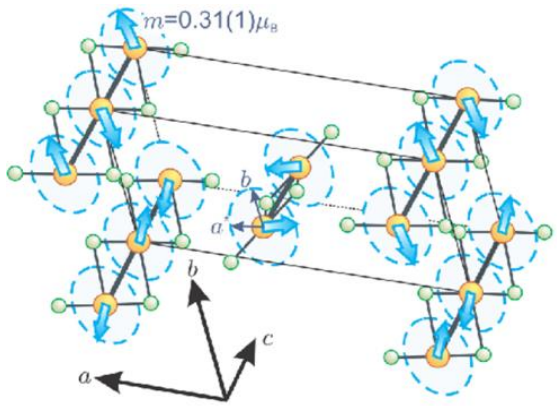

ISSN (ONLINE): 2250-0758, ISSN (PRINT): 2394-6962

Figure 8: Top panel: Neutron-diffraction data from a single crystal of $Cu(py)_2Cl_2$ obtained with the D10 instrument. The main panel depicts the low-temperature scattering intensity (normalized per neutron flux and counting time) as a function of momentum (points) in the (0.5, *K*, 0.5) direction, along with a fit using a collection of Gaussian peaks (solid line)

The temperature dependence of the scattering intensity at the magnetic Bragg reflection is shown in the inset (0.5, 0.4, 0.5). The solid line around T_N serves as a visual aid. Diffraction experiments revealed the spin structure of the $Cu(py)_2Cl_2$ ordered phase in the bottom panel. The system is in a state of rapid oscillation. On this frequency scale, there is no EPR line splitting, which explains why. An unexpected result was found in the magnetic structure when neutron diffraction was used to study it. The material is magnetically organized in three dimensions with an incommensurate magnetic structure below T_N = 1.12 K. The temperature variation of one matching Bragg-peak intensity is shown in the top panel of Fig. 8. The observed magnetic-structure propagation vector is **Q** = ± (0.5, 0.4, 0.5) r.l.u. The structure was solved using 44 magnetic reflections at a base temperature of 100 mK, with scale factors and extinction coefficients calculated using nuclear-peak refinement. We discovered a helicoidally spin arrangement in which the rotation plane is perpendicular to the chain direction (which is perpendicular to the chain direction). (the a b plane). This structure can be seen towards the bottom of the page. Figure 8: panel m = 0.31 (1) μ_B shows that the ordered moment per Cu^{2+} site is greatly reduced. Nonetheless, we should note that this value is still twice as high as the expectation based on mean-field theory. This mismatch is unsurprising because the previously employed mean-field theory is ineffective in the presence of frustration, which, as the authors point out, is common.

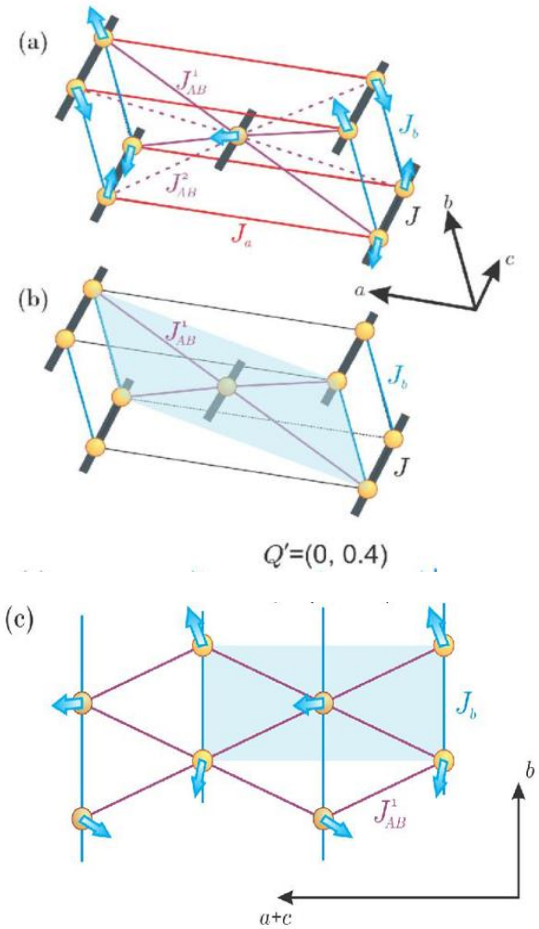

Figure 9: (a) The most general Heisenberg exchange method for $Cu(py)_2Cl_2$.(b) To qualitatively capture the ground state, a minimalistic model is required. (c) A single triangular-lattice layer is projected, as shown in (b)

The facts presented here show that is an important component of the magnetism of $Cu(py)_2Cl_2$.

The presence of Cu^{2+} ions in the A and B positions, linked by a half-period screw translation,

produces a noncollinear magnetic structure in $Cu(py)_2Cl_2$.This results in a semi-body-centered arrangement of magnetic moments within a structural unit cell, with vexing diagonal interactions. The various exchange interactions in $Cu(py)_2Cl_2$are summarized in Fig. 9.(a). The intrachain exchange interaction J is the most important, as it is adequate to characterize thermodynamics and high-energy spectrum characteristics. In addition to the primary exchange interaction, there are two no frustrating interchain contacts, J_a and J_b. These interactions connect the *A*-*A* or *B*-*B* type chains' spins.

Finally, the *A* and *B* sub lattices have inconvenient diagonal interactions. JAB^1 and JAB^2 are two types of such diagonal couplings distinguished by the space group $P2_1/n$. Because the comparable distance between the ions for JAB^1 is around 1% shorter than for JAB^2, one may expect JAB^1 to be slightly stronger within this pair. We feel that this disparity, along with the unique geometric design, is the key to comprehending the strange spiral ground state. As shown in Fig. 9. (b), only JAB^1 and J_b can be considered as toy models for interchain coupling. The triangular layers are then generated in the diagonal planes, with Jb at the base of the triangle and JAB^1 along its sides Fig. 9(c).Then cos (Q · b) = $JAB^1/2J_b$ is the 2D propagation vector within this plane, which is incommensurate only along the b direction. It's worth noting that this incompatibility is caused solely by the rivalry of two weak exchange interactions and not by the intrachain exchange interaction *J*. The comparatively large pitch angle of 108 degrees between the A and B chain sub lattices is due to this. Simultaneously, the strong intrachain contact *J* encourages antiparallel spin arrangement along the c axis, eventually leading to as seen experimentally, this results in the 3D ordering wave vector **Q** = (0.5, Q^b_{inc}, 0.5). While this toy model qualitatively depicts the incommensurate ground state, more density functional theory (DFT) calculations are needed to determine the true hierarchy of the key magnetic interactions and allow for a quantitative description.

The discovery of the incommensurate order not only reveals the frustrated nature of intra chain interactions, but it also asks for a revision of the antiferromagnetic resonance below T_N, as reported by Okuda and Kadowaki. Antiferromagnetic resonance in spiral structures is known to differ from that in simple collinear situations (see, e.g.,). The low magnitude of the ordered moment emphasizes the importance of quantum fluctuations even at energies below T_N, and suggests that distinctive 1D features could be observed at energies above the inter chain coupling.

IV. CONCLUSIONS

The spin-1/2 Heisenberg AF chain compound $Cu(py)_2Cl_2$ was investigated using systematic EPR and neutron diffraction techniques. Anisotropy was found to be quite minimal (δ ~0.04%–0.06% of *J*). The EPR line width's angular dependency clearly shows that inter chain geometrical frustration is a major contributor to the helical magnetic structure found below T_N.

REFERENCES

[1] S. A. Zvyagin, E. Cižmár, M. Ozerov, J. Wosnitza, R. Feyerherm, S. R. Manmana, & F. Mila. (2011). *Phys. Rev. B 83*, 060409(R).

[2] F. H. L. Essler, A. Furusaki, & T. Hikihara, (2004). *Phys. Rev. B* ***68***, 064410.

[3] M. Thede, F. Xiao, Ch. Baines, C. Landee, E. Morenzoni, and A. Zheludev, (2012). *Phys. Rev. B* 86, 180407(R)

[4] A. Validov, M. Ozerov, J. Wosnitza, S. A. Zvyagin, M. M. Turnbull, C. P. Landee, & G. B. Teitel'baum, J. (2014). *Phys. Condens. Matter* ***26(***5), 224-229.

[5] Ali I, Islam MU, Ashiq MN, et al. (2015). Investigation of the magnetic properties of nanometric SrSmCoNi ferrite/PST matri. *Ceram Int.; 41*:8748–8754.

[6] Pullar RC. Hexagonal ferrites: A review of the synthesis, properties and applications of hexaferrite ceramics. *Prog Mater Sci, 57*(7), 349-355.

[7] Yu H. (2016). Bafe12o19 powder with high magnetization prepared by acetone-aided coprecipitation. *J Magn Magn Mater. 341*:79–85.

[8] Chen D, Liu Y, Li Y, et al. (2014). Microstructure and magnetic properties of Al-doped barium ferrite with sodium citrate as chelate agent. *J Magn Magn Mate , 337*-338:65–69.

[9] Topkaya R. (2016). Effect of Zn substitution on temperature dependent magnetic properties of BaFe12O19 hexaferrites. *J Alloy Compd.725*:1230–1237.